High Rayleigh number convection in a porous medium containing a thin low-permeability layer

Duncan R. Hewitt[1,†], Jerome A. Neufeld[1,2,3] and John R. Lister[1]

[1]Department of Applied Mathematics and Theoretical Physics, Institute of Theoretical Geophysics,
University of Cambridge, Wilberforce Road, Cambridge CB3 0WA, UK

[2]Department of Earth Science, University of Cambridge, Cambridge CB2 3EQ, UK

[3]BP Institute, University of Cambridge, Cambridge CB3 0EZ, UK

Porous geological formations are commonly interspersed with thin, roughly horizontal, low-permeability layers. Statistically steady convection at high Rayleigh number Ra is investigated numerically in a two-dimensional porous medium that is heated at the lower boundary and cooled at the upper, and contains a thin, horizontal, low-permeability interior layer. In the limit that both the dimensionless thickness h and permeability Π of the low-permeability layer are small, the flow is described solely by the impedance of the layer $\Omega = h/\Pi$ and by Ra. In the limit $\Omega \to 0$ (i.e. $h \to 0$), the system reduces to a homogeneous Rayleigh–Darcy (porous Rayleigh–Bénard) cell. Two notable features are observed as Ω is increased: the dominant horizontal length scale of the flow increases; and the heat flux, as measured by the Nusselt number Nu, can increase. For larger values of Ω, Nu always decreases. The dependence of the flow on Ra is explored, over the range $2500 \leqslant Ra \leqslant 2 \times 10^4$. Simple one-dimensional models are developed to describe some of the observed features of the relationship $Nu(\Omega)$.

Key words: convection, convection in porous media, porous media

1. Introduction

The convective flow of fluid in porous media plays an important role in a range of environmental and industrial contexts. Recent interest in the subject has been spurred on by the relevance of convection for the long-term security of geologically sequestered CO_2 in deep saline aquifers (Bachu 2008; Zhang 2013; Huppert & Neufeld 2014). Sequestration, which has been widely proposed as a means of mitigating anthropogenic emissions of CO_2 (currently more than 30 billion tons per year; Friedlingstein *et al.* 2010), is achieved by the injection of supercritical CO_2 into brine-saturated porous rock that is typically located at depths of $\gtrsim 800$ m. Being less dense than brine, the injected CO_2 can leak back to the surface through faults in the overlying caprock (e.g. Pritchard 2007; Neufeld *et al.* 2011; Vella *et al.* 2011). One mechanism for more secure storage is the weak dissolution of CO_2 into the

† Email address for correspondence: drh39@cam.ac.uk

underlying brine; dissolution raises the density of the brine, such that the resultant CO_2-saturated solution can be unstable to downwelling convection. Convective flow leads to an enhanced rate of dissolution, and more secure long-term storage. This observation has motivated a large number of studies of the convective dissolution of CO_2, using numerical simulations (e.g. Pau *et al.* 2010; Hewitt, Neufeld & Lister 2013; Szulczewski, Hesse & Juanes 2013; Slim 2014), laboratory experiments (e.g. Kneafsey & Pruess 2010; Neufeld *et al.* 2010; Backhaus, Turitsyn & Ecke 2011; Slim *et al.* 2013), theoretical analysis (e.g. Riaz *et al.* 2006; Daniel, Tilton & Riaz 2013; Tilton & Riaz 2014), and field measurements from naturally occurring CO_2 reservoirs (e.g. Gilfillan *et al.* 2009).

Porous media are often modelled as homogeneous, and described by uniform averaged properties like the porosity and permeability. Natural porous media, however, are rarely homogeneous. In particular, geophysical aquifers commonly consist of a series of roughly horizontal layers of rock of distinctly different permeabilities (Monkhouse 1970; Phillips 2009). Layering of this sort can frequently be observed on exposed rock faces in quarries or coastal cliffs, such as the Jurassic sandstone cliffs at Bridport in Dorset, UK (Morris & Shepperd 1982). Both the permeability and the thickness of layers can be much smaller than those of the main formation: the exposed Aztec sandstone in Nevada, for example, at over a kilometre in depth, is characterized by multiple very thin ($\sim$1 cm) horizontal layers that are several orders of magnitude less permeable than the main formation (Sternlof *et al.* 2006). An important example for the geological storage of CO_2 is the Utsira sand formation at the Sleipner field in the North Sea, where roughly 1 million tonnes of CO_2 have been sequestered every year since 1996 (Bickle *et al.* 2007). Seismic images have revealed that the flow of injected CO_2 is significantly affected by the presence of nine low-permeability roughly horizontal mudstone layers which intersperse the formation, and are much thinner (roughly 1–5 m deep) than the formation itself (roughly 200 m deep) (Bickle *et al.* 2007).

Convection in a homogeneous and isotropic porous medium has been studied in a range of settings (Nield & Bejan 2013). The porous version of the Rayleigh–Bénard cell (known variously as the 'Horton–Rogers', 'Lapwood', Darcy–Bénard', or, as in this paper, 'Rayleigh–Darcy' cell), which consists of a fluid-saturated porous medium with a heated lower boundary and cooled upper boundary, is an archetypal system for the study of statistically steady porous convection. The strength of convection is determined in large part by the Rayleigh number Ra, which is a dimensionless ratio of the buoyancy forces that drive convection to the inhibiting effects of viscosity and diffusion. In a two-dimensional Rayleigh–Darcy cell, there is no convection for $Ra < Ra_{crit} = 4\pi^2$ (Lapwood 1948), while for $4\pi^2 \leqslant Ra \lesssim 1300$, the convective flow takes the form of large-scale rolls. The rolls, which are steady for low values of Ra, are perturbed by a series of secondary instabilities as Ra is increased (Graham & Steen 1994; Otero *et al.* 2004). For $Ra \gtrsim 1300$, the roll structure is broken down completely, and there is a transition in the flow to the 'high-Ra' regime (Otero *et al.* 2004; Hewitt, Neufeld & Lister 2012). The flow in this regime is characterized in the interior of the cell by vertical columnar 'megaplumes' with a statistically regular horizontal wavelength. The megaplumes are driven near to the upper and lower boundaries of the cell by vigorous short-wavelength boundary-layer instabilities or 'protoplumes' (Hewitt *et al.* 2012). Curiously, the interior flow becomes increasingly 'ordered' as Ra is increased, and the average horizontal wavenumber k of the flow is roughly fitted by $k \sim Ra^{0.4}$ for $1300 \lesssim Ra \leqslant 4 \times 10^4$. Over this same range, the convective flux, as measured by the dimensionless Nusselt number Nu, is extremely

well described by the empirical fit $Nu = \alpha Ra + \beta$, for $\alpha = 6.9 \times 10^{-3}$ and $\beta = 2.75$ (Hewitt *et al.* 2013). Similar behaviour has been observed in three dimensions (Hewitt, Neufeld & Lister 2014). The high-Ra regime is relevant in geophysical contexts: estimates of Ra for the convective dissolution of CO_2 in a typical high-permeability aquifer, such as at Sleipner, give values of $Ra = O(10^4)$, or even larger (see e.g. Bickle *et al.* 2007; Hewitt *et al.* 2013 for approximate parameter values).

The study of convection in inhomogeneous or anisotropic media, however, has tended to focus on the onset of convection and the subsequent dynamics of the flow at low Rayleigh numbers (e.g. Simmons, Fenstemaker & Sharp 2001; Ennis-King, Preston & Paterson 2005; Rapaka *et al.* 2009; Nield & Bejan 2013). For media comprising alternate layers of high and low permeability, McKibbin & O'Sullivan (1980, 1981) found that, as the permeability contrast between the layers is increased, there is a transition in the flow dynamics from large-scale convective rolls to local convective structures confined to the higher-permeability layers. Rees & Riley (1990) studied the effect of layering in a three-dimensional medium on convection patterns using weakly nonlinear stability analysis. McKibbin & Tyvand (1983) examined the flow at low Ra in a medium containing a series of thin low-permeability horizontal layers, while Genç & Rees (2011) considered the limit of an impermeable and infinitesimally thin horizontal barrier in an otherwise homogeneous cell. In both cases, the critical Rayleigh number for the onset of convection was found to increase significantly from the homogeneous case. McKibbin & Tyvand (1983) modelled the flow under the assumption that both the thickness and the permeability of the low-permeability layers were small but their ratio was $O(1)$; we adopt a similar approach here for the case of vigorous high-Ra convection.

In this paper, we use high-resolution numerical simulations to examine the impact of a thin horizontal low-permeability layer on the strength and dynamical structure of high-Ra porous convection. We consider a cell comprising identical upper and lower layers, between which there is a thin interior layer of a lower permeability. The upper and lower layers have equal depth, such that the low-permeability layer is located at the centre of the cell. The whole cell is heated from below and cooled from above. The flow thus attains a statistically steady state, which allows a systematic examination of the effect of a thin low-permeability layer on the heat flux through the cell and on the associated flow structure. In the limit in which there is no low-permeability layer, the cell is identical to the homogeneous Rayleigh–Darcy cell discussed above. All physical properties of the fluid and the medium except the permeability are assumed to be constant throughout the cell; in particular, we assume for simplicity that the porosity ϕ of the medium is uniform, and is thus independent of the permeability (see appendix A for a discussion of this assumption). To aid intuition, and in common with most previous studies of statistically steady convection, we consider thermal convection in this paper using an assumption of local thermal equilibrium between the solid and liquid phase. However, the work is equally applicable to compositional convection, as discussed in § 2, which is the case of interest for the convective dissolution of CO_2.

The paper is laid out as follows. In § 2, we present the governing equations and non-dimensionalization. In § 3, we discuss our numerical results. We show that, in the limit that both the dimensionless thickness h and permeability Π of the low-permeability layer are small, the flow can be described solely by their ratio $\Omega = h/\Pi$. In § 3.4, we examine in detail the dependence on Ω of the dynamical structure of the flow and the flux Nu, and in § 3.5 we investigate the dependence of the flow on Ra, across the range $2500 \leqslant Ra \leqslant 2 \times 10^4$. In § 4, we develop simple one-dimensional models of the

(a)

$z^* = H$ ——————— $T^* = T_0$ ———————

K_1

$z^* = z_2^*$

$z^* = z_1^*$

K_2 $\rceil h^*$

K_1

$z^* = 0$ ——————— $T^* = T_0 + \Delta T$

(b)

$z = 1$ ——————— $T = 0$ ———————

1

$z = z_2$

$z = z_1$
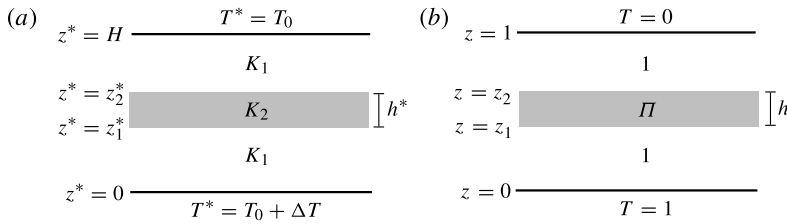
Π $\rceil h$

1

$z = 0$ ——————— $T = 1$

FIGURE 1. A schematic showing the layered system under consideration, with the permeability of each layer and the thermal boundary conditions marked. (a) Dimensional variables. (b) Dimensionless variables.

system that capture some of the observed features of the relationship $Nu(\Omega)$, and we discuss the limitations of the models. Finally, in §5, we summarize and discuss our main results.

2. Governing equations

We consider the flow of a Boussinesq fluid in a two-dimensional porous medium, with horizontal and vertical coordinates x^* and z^* respectively. The medium comprises a thin interior layer sandwiched between relatively deep upper and lower layers (figure 1a). The combined depth of the three layers is $z^* = H$. The upper and lower layers have uniform permeability K_1, while the thin interior layer has uniform permeability $K_2 < K_1$ and depth $h^* \ll H$, and lies between $z_1^* = (H - h^*)/2$ and $z_2^* = (H + h^*)/2$. Within each layer, the medium is homogeneous and isotropic.

We assume that the flow $\boldsymbol{u}^* = (u^*, w^*)$ in all three layers is incompressible and is governed by Darcy's law. The temperature field T^* is assumed to be locally equilibrated between the solid and the liquid phases. The equation of state $\rho^*(T^*)$ is linear and T^* satisfies an advection–diffusion transport equation. These equations are given by

$$\nabla \cdot \boldsymbol{u}^* = 0, \tag{2.1a}$$

$$\mu \boldsymbol{u}^* = \begin{cases} -K_1(\nabla p^* + \rho^* g \hat{\boldsymbol{z}}), & 0 \leqslant z^* \leqslant z_1^*, \ z_2^* \leqslant z^* \leqslant H, \\ -K_2(\nabla p^* + \rho^* g \hat{\boldsymbol{z}}), & z_1^* < z^* < z_2^*, \end{cases} \tag{2.1b}$$

$$\rho^* = \rho_0 \left[1 - a \left(T^* - T_0 \right) \right], \tag{2.1c}$$

$$\frac{[\phi \rho_l c_l + (1 - \phi) \rho_s c_s]}{\rho_l c_l} \frac{\partial T^*}{\partial t^*} + \boldsymbol{u}^* \cdot \nabla T^* = \kappa \nabla^2 T^*, \tag{2.1d}$$

where μ is the viscosity, p^* is the pressure, g is the gravitational acceleration, $\hat{\boldsymbol{z}}$ is a unit vector in the z^* direction, ρ_0 and T_0 are a constant reference density and temperature, respectively, a is the coefficient of thermal expansion, ϕ is the constant porosity of the medium, κ is the constant average thermal diffusivity, and ρ_i and c_i are the densities and specific heats of the liquid ($i = l$) or solid ($i = s$) phases. A brief discussion of the effect of a different porosity and thermal diffusivity in the low-permeability layer is given in appendix A. Note that these equations are equally applicable to compositionally driven convection if we set $c_s = 0$ and take $D = \kappa/\phi$ to be the constant solutal diffusivity in the liquid phase.

On the upper and the lower boundaries of the domain, the vertical velocity vanishes and a fixed temperature is imposed, such that

$$T^*|_{z^*=0} = T_0 + \Delta T, \quad T^*|_{z^*=H} = T_0, \quad w^*|_{z^*=0,H} = 0, \tag{2.2a–c}$$

where ΔT is a fixed unstable (positive) temperature difference. The pressure, temperature and normal velocity are continuous at the internal boundaries $z^* = z^*_{1,2}$.

We non-dimensionalize the system with respect to the depth H of the whole domain, the permeability K_1 of the upper and lower layers, the density difference across the domain $\Delta\rho = \rho_0 a \Delta T$, the buoyancy-velocity scale $U = g\Delta\rho K_1/\mu$, and the convective time scale $[\phi\rho_l c_l + (1 - \phi)\rho_s c_s]H/(\rho_l c_l U)$. The dimensionless rescaled temperature is given by $T = (T^* - T_0)/\Delta T$. In dimensionless variables, the governing equations (2.1) reduce to

$$\nabla \cdot \boldsymbol{u} = 0, \tag{2.3a}$$

$$\boldsymbol{u} = \begin{cases} -(\nabla p - T\hat{\boldsymbol{z}}), & 0 \leqslant z \leqslant z_1, \ z_2 \leqslant z \leqslant 1, \\ -\Pi(\nabla p - T\hat{\boldsymbol{z}}), & z_1 < z < z_2, \end{cases} \tag{2.3b}$$

$$\frac{\partial T}{\partial t} + \boldsymbol{u} \cdot \nabla T = \frac{1}{Ra}\nabla^2 T, \tag{2.3c}$$

where $p = (p^* + \rho_0 g z^*)/(\Delta\rho g H)$ is a reduced pressure, $\Pi = K_2/K_1 < 1$ is the ratio of the two permeabilities, and we have combined (2.1b) and (2.1c). The dimensionless edges of the interior low-permeability layer are given by $z_{1,2} = (1 \mp h)/2$. The parameter Ra is the Rayleigh number, which is the ratio of the driving strength of buoyancy to the inhibiting dissipative effects of viscosity and diffusion, and is given by

$$Ra = \frac{g\Delta\rho K_1 H}{\kappa\mu}. \tag{2.4}$$

Since we have non-dimensionalized with respect to the convective, rather than the diffusive, time scale, the Rayleigh number appears in (2.3c) as an inverse diffusivity.

The dimensionless boundary conditions on the upper and lower boundaries of the domain are given from (2.2) by

$$T|_{z=0} = 1, \quad T|_{z=1} = 0, \quad w|_{z=0,1} = 0 \tag{2.5a–c}$$

(figure 1b). The conditions at the internal interfaces between the different layers are given by continuity of temperature, pressure and normal velocity,

$$[T] = [p] = [w] = 0 \quad \text{at } z = z_1, z_2. \tag{2.6}$$

Incompressibility (2.3a) is satisfied by the introduction of a streamfunction ψ which obeys $(u, w) = (\partial\psi/\partial z, -\partial\psi/\partial x)$. We eliminate the pressure field by taking the curl of (2.3b), which gives

$$\nabla^2\psi = \begin{cases} -\partial T/\partial x, & 0 \leqslant z \leqslant z_1, \ z_2 \leqslant z \leqslant 1, \\ -\Pi \, \partial T/\partial x, & z_1 < z < z_2. \end{cases} \tag{2.7}$$

We incorporate the continuity conditions on the pressure at the internal interfaces by combining (2.6) with Darcy's law (2.3b), to re-express the conditions in terms of discontinuities of the horizontal velocity:

$$u|_{z=z_1^+} = \Pi u|_{z=z_1^-}, \quad u|_{z=z_2^-} = \Pi u|_{z=z_2^+}. \tag{2.8a,b}$$

The flow is described by three dimensionless parameters: the Rayleigh number Ra; the permeability ratio Π; and the relative thickness of the low-permeability layer $h = h^*/H$. The statistically steady convective flux, or, in dimensionless variables, the Nusselt number $Nu(Ra, \Pi, h)$, can be defined as the temporally and horizontally averaged heat flux at any height z, and is here given by

$$Nu = \langle nu(t) \rangle = \left\langle -\frac{1}{L} \int_0^L \left. \frac{\partial T}{\partial z} \right|_{z=0} \mathrm{d}x \right\rangle, \tag{2.9}$$

where $nu(t)$ is the instantaneous flux through the lower boundary at a given time t, and L is the aspect ratio of the cell. The angle brackets $\langle \rangle$ signify a long-time average.

We solved (2.3c) and (2.7) numerically. The numerical method is discussed very briefly here and described in more detail in appendix B. We imposed periodic boundary conditions on the cell in the x direction at $x = 0, L$. Unless otherwise stated, all the numerical results presented in this paper have aspect ratio $L = 4$. We employed a vertical coordinate transformation in order to fully resolve both the thin boundary layers at the upper and lower boundaries of the domain, and the interfaces between the different layers inside the cell. The initial condition for all calculations, unless explicitly noted in the text, was given by a linear vertical temperature gradient with a small random perturbation. After an initial period of reorganization, the flow attains a statistically steady state. At high Ra, the local flux through the boundary $nu(t)$ exhibits chaotic fluctuations about a mean in this state, and the computations are continued until the Nusselt number (2.9) has converged to within 0.25 % of its mean.

3. Numerical results

In this section we present our numerical results and discuss the observations. We focus initially in §§ 3.1–3.4 on simulations at $Ra = 5000$, which is an appreciably higher value than the onset of the high-Ra regime for homogeneous Rayleigh–Darcy convection at $Ra \approx 1300$ (Otero *et al.* 2004; Hewitt *et al.* 2012). We then examine the dependence of the system on Ra in § 3.5. The effects of the interior low-permeability layer on the convective dynamics is more complicated than might be anticipated, and thus we describe the observations in some detail. A summary of the main observations is given in § 3.6.

3.1. *Numerical results for $Ra = 5000$*

Snapshots of the statistically steady temperature field for different values of the thickness h of the low-permeability layer and two different permeability ratios Π are shown in figures 2 and 3. The homogeneous case $h = 0$ (equivalently $\Pi = 1$) is shown in figure 2(*a*).

The structure of the flow changes significantly as the thickness of the low-permeability layer increases. For homogeneous convection (figure 2*a*), the flow is dominated away from the boundaries by columnar megaplumes with a roughly regular horizontal wavelength (Hewitt *et al.* 2012). The horizontal scale of these plumes increases significantly as h is increased (figure 2*b–f*). The flow increasingly resembles an ordered array of cells, each of which is half the height of the domain and comprises a thin vertical plume flowing up/down and a much wider plume carrying the return flow. For the smaller value of Π (figure 3), the horizontal scale of the flow increases even more rapidly as h is increased. In fact, for sufficiently
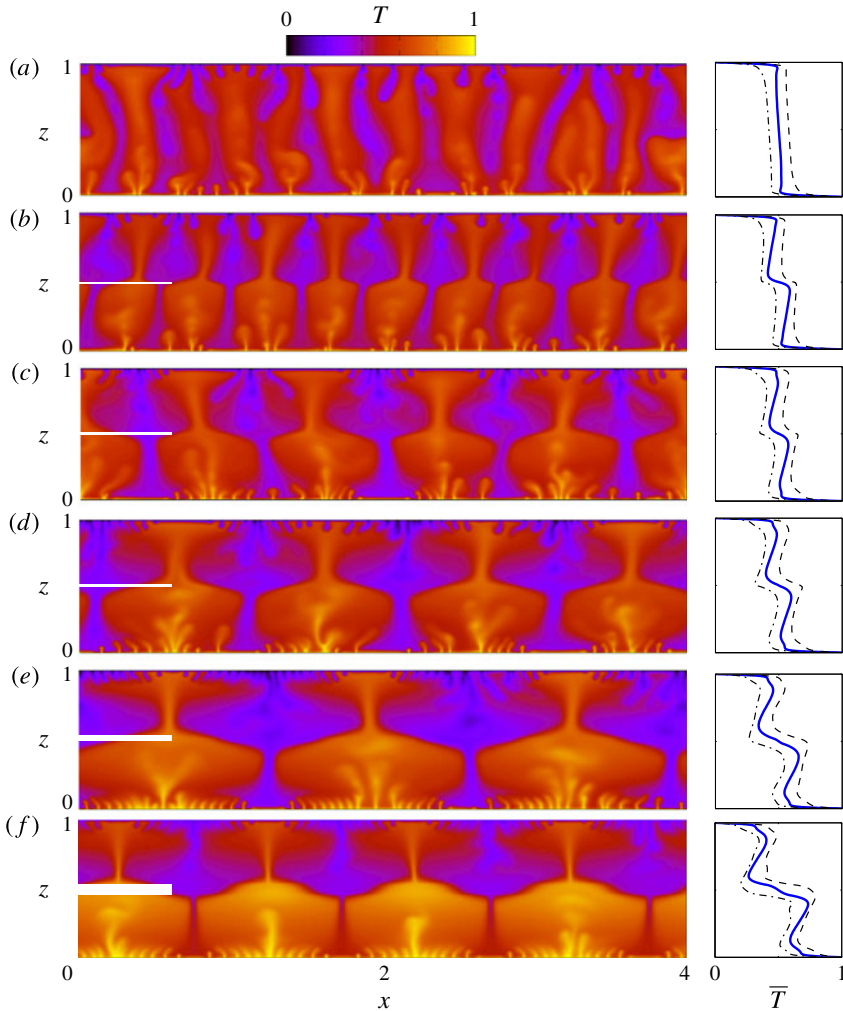
FIGURE 2. (Colour online) Snapshots of the temperature field T for $Ra = 5000$, $\Pi = 0.04$, and varying thickness h of the low-permeability layer: (a) $h = 0$ (no low-permeability layer), (b) $h = 0.005$, (c) $h = 0.01$, (d) $h = 0.02$, (e) $h = 0.04$, and (f) $h = 0.08$. The white bars on the left mark the location and thickness of the low-permeability layer. The temporally and horizontally averaged temperature $\overline{T}(z)$ (solid) is shown on the right-hand side, together with the temperature averaged only over fluid with $w > 0$ (dashed) and only over fluid with $w < 0$ (dot-dashed).

large values of h, the horizontal scale of the plumes appears to have become so broad that protoplumes form near the low-permeability layer (figure 3c–e). There is significant variability in the structure of the flow between different simulations, as exemplified by figure 2(e,f) which, contrary to the general trend just discussed, show a flow with $h = 0.08$ which has a smaller horizontal length scale than a flow with $h = 0.04$.

Profiles of the horizontally and temporally averaged temperature $\overline{T}$ (figures 2, 3) show that the temperature difference across the low-permeability layer increases as h is increased. The background stratification also appears to depend on h: for
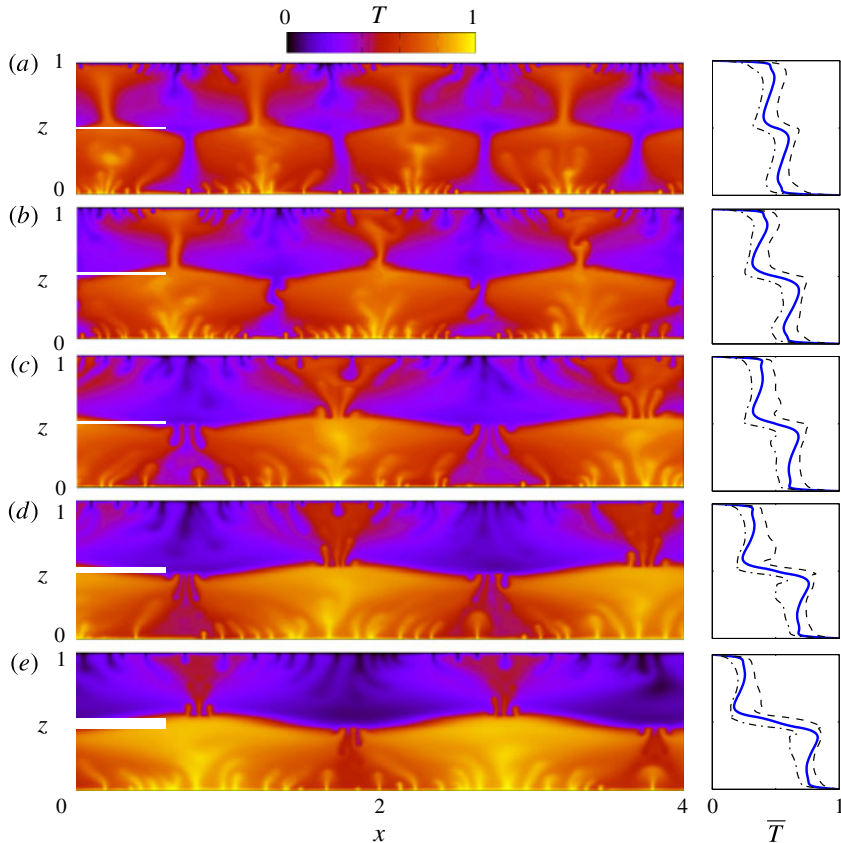
FIGURE 3. (Colour online) Snapshots of the temperature field T for $Ra = 5000$, $\Pi = 0.01$, and varying thickness of the low-permeability layer: (*a*) $h = 0.005$, (*b*) $h = 0.01$, (*c*) $h = 0.02$, (*d*) $h = 0.04$, and (*e*) $h = 0.08$. The white bars on the left mark the location and thickness of the low-permeability layer. Profiles of $\overline{T}(z)$ (solid) are shown on the right-hand side, together with the temperature averaged only over fluid with $w > 0$ (dashed) and only over fluid with $w < 0$ (dot-dashed).

homogeneous convection (figure 2*a*), the profile has a very weak negative gradient throughout the interior of the domain, whereas, as h is increased, (figures 2*b–f* and 3), the gradient becomes positive, giving an apparent stable background stratification in each layer. Profiles of the average temperature restricted to either the upwelling or the downwelling regions alone (figures 2, 3 dashed and dot-dashed lines) do not show as large a stratification as the full profiles of $\overline{T}$, although the fluid is still slightly stratified, particularly in the plumes that carry fluid towards the low-permeability layer.

In any simulation, we find that there are always an equal number of upwelling and downwelling plumes, and that the plumes are aligned on either side of the low-permeability layer such that an upwelling plume in the lower layer lies directly below an upwelling plume in the upper layer. As might be also expected from the geometry, the numerical results show a symmetry about $z = 0.5$, such that, provided the results are averaged over sufficiently long times, the profiles of $\overline{T}$ are invariant under the transformations $z \to 1 - z$ and $\overline{T} \to 1 - \overline{T}$.
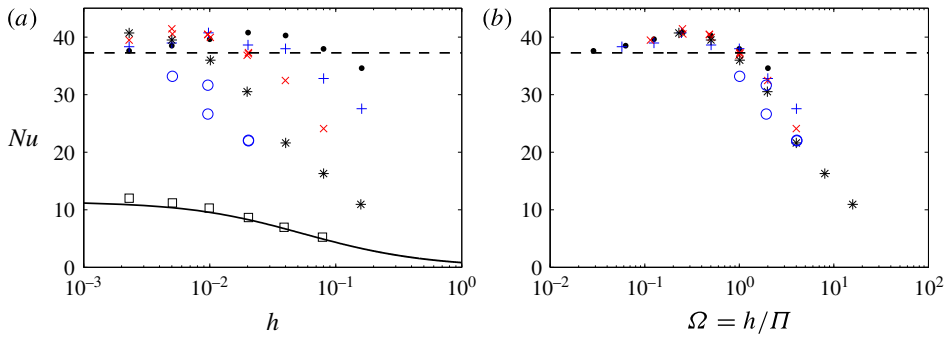
FIGURE 4. (Colour online) The Nusselt number Nu for $Ra = 5000$: (a) as a function of the thickness h of the low-permeability layer, and (b) as a function of the impedance $\Omega = h/\Pi$, where Π is the permeability ratio. The data points are for $\Pi = 0$ (squares), $\Pi = 0.005$ (circles), $\Pi = 0.01$ (stars), $\Pi = 0.02$ (crosses), $\Pi = 0.04$ (pluses), $\Pi = 0.08$ (dots). The solid line in (a) is the theoretical prediction for an impermeable interior layer (see §4.2). For homogeneous convection (i.e. the limit $h \to 0$), $Nu = 37.25$ (dashed line, taken from Hewitt *et al.* 2012). Surprisingly, the Nusselt number initially increases with Ω, before decreasing for $\Omega \gtrsim 0.25$.

Figure 4(a) shows the Nusselt number as a function of the thickness h of the low-permeability layer for different values of Π and for an impermeable layer ($\Pi = 0$). Surprisingly, Nu does not decrease monotonically as h is increased, as might be expected from the increasing proportion of the domain that is occupied by low-permeability material. Instead, Nu first increases for small h ($\Pi \neq 0$), before decreasing for larger h. The data for $\Pi \neq 0$ roughly collapse onto a single curve when plotted as a function of the quantity $\Omega = h/\Pi$ (figure 4b), as discussed in the following section. The case $\Pi = 0$ is quite different since all the heat flux across an impermeable layer must be by diffusion.

3.2. *Dependence on* $\Omega = h/\Pi$

The Nusselt number collapses onto a single curve as a function of $\Omega = h/\Pi$ (figure 4b). This dependence can be simply understood by examination of the governing equations for $h, \Pi \ll 1$. In this limit, Darcy's law (2.3b) implies that the horizontal velocity in the low-permeability layer is small ($O(\Pi)$), while the vertical velocity is $O(\Pi/h)$ and given by

$$w = -\Pi \left(\frac{\partial p}{\partial z} - T \right) = -\frac{\Pi}{h}[p(z_2) - p(z_1) + O(h)]. \tag{3.1}$$

The flow through the low-permeability layer is therefore predominantly vertical if $h, \Pi \ll 1$ and $\Pi/h = O(1)$, and it is driven by pressure differences, rather than by buoyancy. In this limit, the flow is controlled by the parameter $\Omega = h/\Pi$, which is a form of impedance, being a ratio of pressure difference and Darcy velocity.

We can parameterize the effect of the low-permeability layer in the distinguished limit $h, \Pi \to 0$ with the impedance $\Omega = h/\Pi$ remaining finite. The derivative of (3.1) with respect to x and the continuity conditions for w and p from (2.6) give

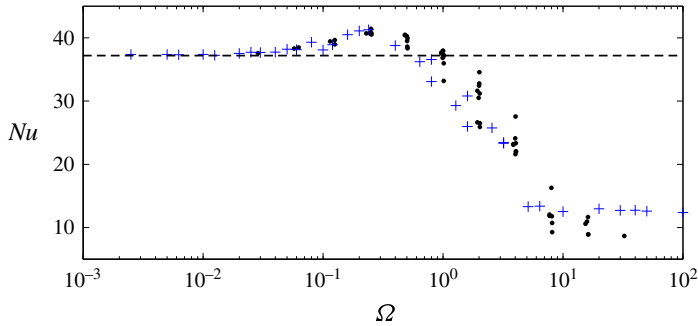$$\Omega \frac{\partial w}{\partial x} \approx u(z_{2+}) - u(z_{1-}). \tag{3.2}$$

FIGURE 5. (Colour online) The Nusselt number $Nu(\Omega) = Nu(h/\Pi)$ from full simulations for $10^{-3} \leqslant h \leqslant 0.2$ and $10^{-4} \leqslant \Pi \leqslant 0.1$ (dots; includes the data from figure 4) and from reduced simulations (pluses) for $Ra = 5000$. The results give good agreement, and tend to the homogeneous value $Nu = 37.25$ (dashed line) in the limit $\Omega \to 0$.

We note that there is no requirement of continuity for the horizontal velocity u at $z = z_{1,2}$. In the limit $h, \Pi \to 0$, (3.2) reduces to a jump condition for u, given by

$$\Omega \left.\frac{\partial w}{\partial x}\right|_{z=0.5} = [u]_{z=0.5_-}^{z=0.5_+}. \tag{3.3}$$

The temperature and vertical velocity are continuous at $z = 0.5$ in this limit.

3.3. *Reduced numerical simulations*

Motivated by the results of the previous section, we developed a simplified numerical scheme in which the thin low-permeability layer is parameterized by the jump condition (3.3), together with continuity of temperature and vertical velocity, at $z = 0.5$ (see appendix B for details). This parameterization both simplifies the numerical computations and appreciably reduces the numerical cost, as there is no longer a low-permeability layer to be resolved. We refer to these simulations as 'reduced', to distinguish from 'full simulations' in which the low-permeability layer is fully represented and resolved.

Calculations of $Nu(\Omega)$ from reduced simulations give good agreement with results from full simulations for different values of h and Π (figure 5). The slight difference in some of the data at large values of Ω is because of the relatively large values of h in some of the full simulations. There is also some scatter in the data, which is related to variability in the horizontal structure of the flow, as discussed in § 3.4.2 below.

Figure 5 shows that Nu increases gradually with Ω to give a maximum of $Nu \approx 41.2$ at $\Omega \approx 0.25$. This is an increase of approximately 10 % from the value of Nu for homogeneous convection. For $\Omega \gtrsim 0.25$, Nu decreases rapidly. For $\Omega \gtrsim 5$, the results from reduced simulations level off at roughly a quarter of the value of Nu for homogeneous convection, while the results from full simulations appear to continue to decrease slowly.

3.4. *The dynamical structure of the flow*

We have observed that the dynamical structure of the flow changes significantly with h and Π (figures 2, 3), and we showed in § 3.2 that the flow is a function of $\Omega = h/\Pi$ only, for $h, \Pi \ll 1$. In this section, we describe in detail the change in the flow with Ω, and the corresponding form of $Nu(\Omega)$.
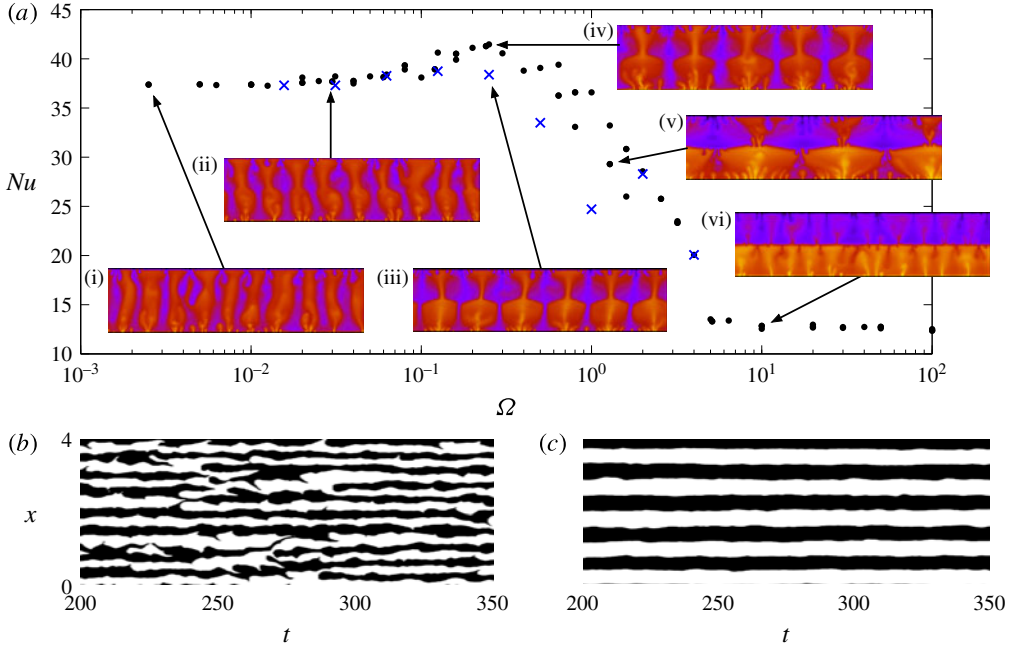
FIGURE 6. (Colour online) (*a*) Calculations of $Nu(\Omega)$ for $Ra = 5000$ from a series of reduced simulations with initial condition given by a small random perturbation to a vertically linear base state (dots; includes the data from figure 5), and from a series of reduced simulations for increasing Ω in which the initial condition for each value of Ω was given by the final state from the previous value (crosses). Snapshots (i)–(v) of the statistically steady-state temperature field for different values of Ω illustrate the increase in the horizontal wavelength with Ω. Snapshot (vi) shows the different flow structure for $\Omega \gtrsim 5$. Snapshots (iii) and (iv) illustrate the effects of hysteresis on the flow structure and on Nu (see § 3.4.2). (*b,c*) Spatio-temporal plots of the sign of the vertical velocity at $z = 0.5$, for: (*b*) $\Omega = 2.5 \times 10^{-3}$, corresponding to snapshot (i); and (*c*) $\Omega = 0.25$, corresponding to snapshot (iv).

3.4.1. *Dependence on Ω*

For $\Omega \lesssim 0.05$ (figure 6*a*: i and ii), the flow resembles homogeneous flow. The dynamics is dominated by predominantly vertical columnar flow across the full height of the domain with a fairly small wavelength. The average widths of upwelling and downwelling plumes are roughly equal throughout the domain, although there are substantial fluctuations in the location of the edges of the columnar megaplumes (figure 6*b*). The Nusselt number does not change appreciably for $\Omega \lesssim 0.05$.

For $0.05 \lesssim \Omega \lesssim 0.3$ (figure 6*a*: iii and iv), the flow increasingly resembles a series of cells of half the height of the domain. In the lower layer, the cells take the form of a wide hot upwelling plume neighbouring a much thinner cold downwelling plume. As the upwelling plume impinges on the low-permeability layer, some fluid spreads laterally and is entrained into the downwelling return flow, while some 'leaks' through into the upper layer and feeds the base of a thin upwelling plume there. The cells have a complementary form in the upper layer. As Ω is increased in this range, the horizontal length scale of the flow increases significantly. The flow also appears to become increasingly 'ordered', in that there is much less temporal variability in the
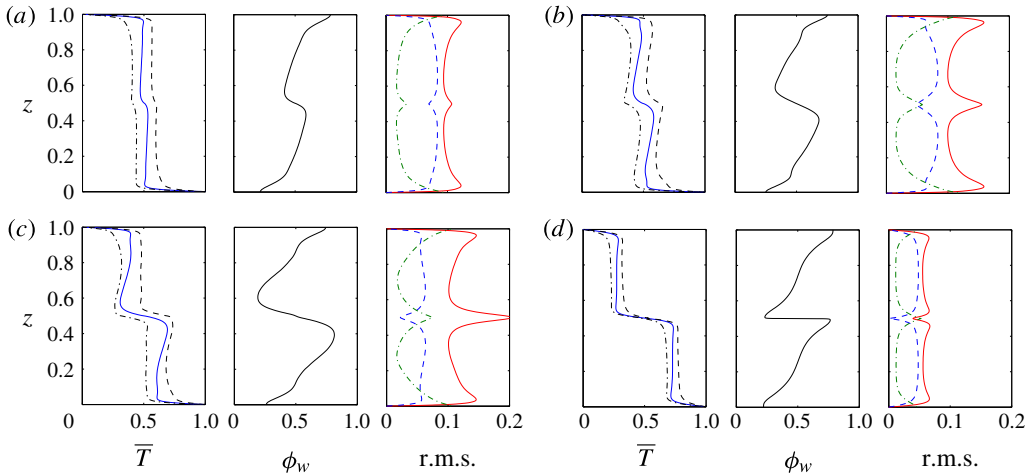
FIGURE 7. (Colour online) Data from reduced simulations at $Ra = 5000$. Left-hand panels show $\overline{T}(z)$ (solid), together with the average temperature of upwelling fluid (dashed) and the average temperature of downwelling fluid (dot-dashed). Centre panels show the temporally averaged proportion ϕ_w of the fluid with $w > 0$, which reveals the asymmetry between the widths of upwelling and downwelling plumes. Right-hand panels show the temporally averaged r.m.s. temperature perturbations $T_{rms}(z)$ (solid) and velocities $w_{rms}(z)$ (dashed) and $u_{rms}(z)$ (dot-dashed). (a) $\Omega = 0.04$, (b) $\Omega = 0.25$, (c) $\Omega = 1.28$, and (d) $\Omega = 10$; corresponding to figure 6(a) (ii), (iv), (v), and (vi), respectively. All the time-averaged results exhibit a reflectional symmetry in the line $z = 0.5$ under the transformations $T \rightarrow 1 - T$ and $w \rightarrow -w$.

location and width of the plumes than at lower values of Ω (figure 6c). The Nusselt number increases over this range of Ω, which is surprising since, for fixed thickness h, this implies that the flux increases as the permeability of the low-permeability layer is decreased.

For $0.3 \lesssim \Omega \lesssim 5$ (figure 6a: v), the horizontal length scale of the flow continues to increase. In this range, the horizontal flow along the boundary of the low-permeability layer appears to be unstable to the growth of protoplumes, which perturb the cellular structure of the flow. The Nusselt number decreases markedly in this range of Ω.

At $\Omega \approx 5$, the structure of the flow changes completely. For $\Omega \gtrsim 5$ (figure 6a: vi), the flow resembles two layers of homogeneous columnar convection, each of half the original height and half the original temperature contrast, placed one on top of the other. Unlike at lower values of Ω, there are no plumes that reach across the full height of the domain. The Nusselt number appears to be roughly constant for $\Omega \gtrsim 5$.

Figure 7 shows four sets of temporally averaged data from reduced simulations, with each set at a value of Ω selected to be in one of the ranges discussed above. For $\Omega = 0.04$ (figure 7a), $\overline{T}$ is roughly uniform in the interior of the domain, except for a small temperature difference across the interior boundary at $z = 0.5$. Similarly, the temperature fluctuations and velocities are fairly uniform, with some small deviations near $z = 0.5$.

For $\Omega = 0.25$ and $\Omega = 1.28$ (figure 7b,c), the temperature difference across the low-permeability layer is larger than in figure 7(a), and the root-mean-square (r.m.s.) quantities vary appreciably near $z = 0.5$. The average temperature field $\overline{T}$ has a weak stable stratification in the upper and lower layers of the domain. There is a notable
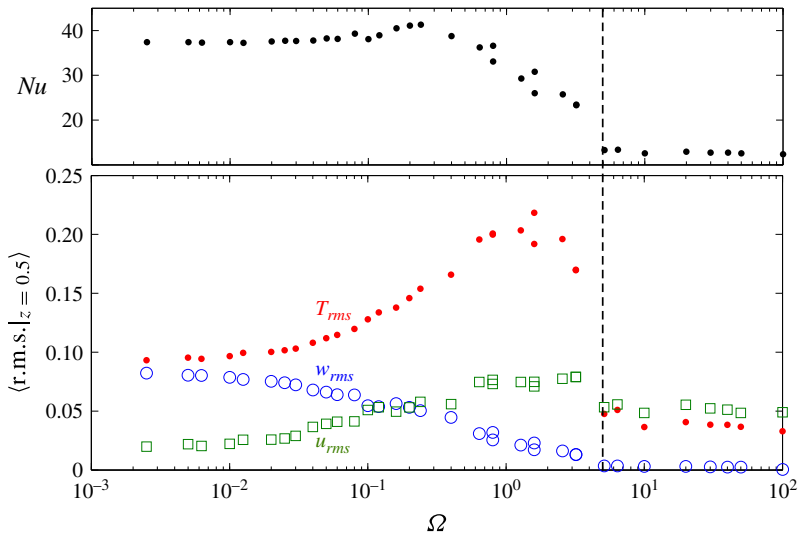
FIGURE 8. (Colour online) Calculations of the temporally averaged r.m.s. temperature perturbations and velocities at $z = 0.5$ from reduced simulations at $Ra = 5000$. The Nusselt number $Nu(\Omega)$ from figure 5 is shown above for comparison. The vertical velocity at $z = 0.5$ is approximately zero for $\Omega \gtrsim 5$; this reflects the transition (dashed line) from dominantly advective to dominantly diffusive transport across the low-permeability layer.

asymmetry between upwelling and downwelling plumes which varies with depth, and the average temperature restricted to either upwelling or downwelling regions alone does not display as strong a stratification as $\overline{T}$. These observations suggest that the apparent stratification is largely a reflection of the variation in the proportion of hot upwelling and cold downwelling fluid with height.

For $\Omega = 10$ (figure 7d), the profiles look quite different. There is negligible apparent stratification in either layer; the vertical velocity nearly vanishes at $z = 0.5$; and the magnitude of the r.m.s. quantities throughout the domain is much less than at lower values of Ω.

As the impedance Ω is increased, the vertical velocity w_{rms} at $z = 0.5$ decreases (figure 8), while the horizontal velocity u_{rms} and temperature fluctuations T_{rms} increase. The trends in w_{rms} and u_{rms} indicate that, as Ω is increased, a larger proportion of the flow that impinges on the low-permeability layer spreads laterally into the return flow rather than 'leaking' across the layer. The marked increase in T_{rms} with Ω may be related to the increased tendency towards forming protoplumes near to the low-permeability layer, though the time scales associated with instability also depend on the balance of velocities.

There is a clear change in the trend of the r.m.s. calculations at $\Omega \approx 5$ (figure 8). In particular, $w_{rms} \approx 0$ for $\Omega \gtrsim 5$, which means that there is no appreciable advective flux through the low-permeability layer. We interpret the change in the dynamics as a transition from advection to diffusion as the dominant transport mechanism across the low-permeability layer. For convenience, we will refer to the regime for $\Omega \gtrsim 5$ as the 'diffusion regime', and to the regime for $\Omega \lesssim 5$ as the 'advection regime'.
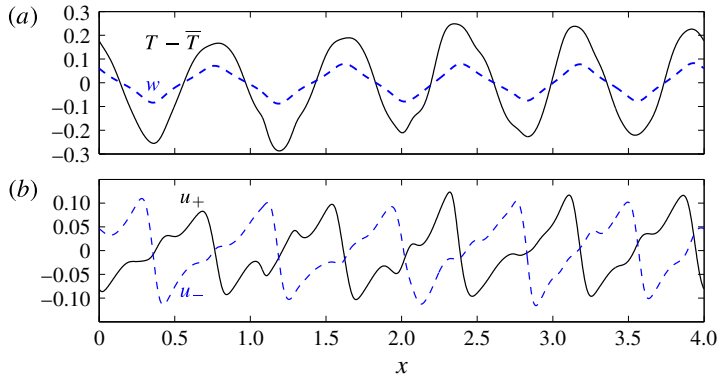
FIGURE 9. (Colour online) Horizontal profiles taken from a reduced simulation at $Ra = 5000$ and $\Omega = 0.25$. (*a*) The temperature variation $T - \overline{T}$ (solid) and the vertical 'leakage' velocity w (dashed) at $z = 0.5$. (*b*) The horizontal velocities u_+ (solid) immediately above the low-permeability layer, and u_- (dashed) immediately below the low-permeability layer.

3.4.2. *Hysteresis*

We observed some variation in the calculations of $Nu(\Omega)$ between simulations at the same value of Ω started with different random perturbations to the same initial state (figure 6*a*, dots). We also observed systematic differences between series of simulations with different initial states (figure 6*a*, dots and crosses). The differences in $Nu(\Omega)$ appear to be related to differences in the number of cells in the domain, as can be seen by a comparison of two flow structures at $\Omega = 0.25$ (figure 6*a*: iii and iv). The fact that there can be different numbers of cells for the same value of Ω is likely to be due to the restriction imposed by the horizontal periodicity of the domain. Once the flow develops a particular structure, we find that the structure can persist as an apparently statistically steady state for a long time.

3.4.3. *Profiles at the low-permeability layer*

Figure 9 shows profiles of the temperature variation and velocities at $z = 0.5$ at $\Omega = 0.25$. The vertical 'leakage' velocity w through the low-permeability layer forms a clear piecewise-linear triangular profile (figure 9*a*). Simulations from across the range $0.05 \lesssim \Omega \lesssim 5$ show similar linear profiles for w. The temperature variation $T - \overline{T}$ is in phase with w, but has a more rounded profile.

The horizontal velocities u_+ and u_- just above and just below the low-permeability layer (at $z = 0.5^+$ and $z = 0.5^-$), respectively, form an offset repeating sawtooth profile (figure 9*b*). The profiles reveal something of the cellular structure of the flow. In the upper half of the domain, for example, hot fluid that has leaked up across the layer is swept laterally as a buoyant boundary layer and converges into thin regions where u_+ changes rapidly from positive to negative (figure 9*b*). These regions, which are also centred on the positive maxima of the leakage velocity w (figure 9*a*), correspond to thin upwelling plumes. In the regions between the thin upwelling plumes there are broad regions of downwelling relatively cold fluid, which impinge on the low-permeability layer and are deflected into the lateral flow discussed above, roughly like a stagnation-point flow. The flow in the lower half of the domain has a complementary form, offset laterally by half a period, such that the thin upwelling plumes in the upper half of the domain lie above the broad upwelling regions in the lower half of the
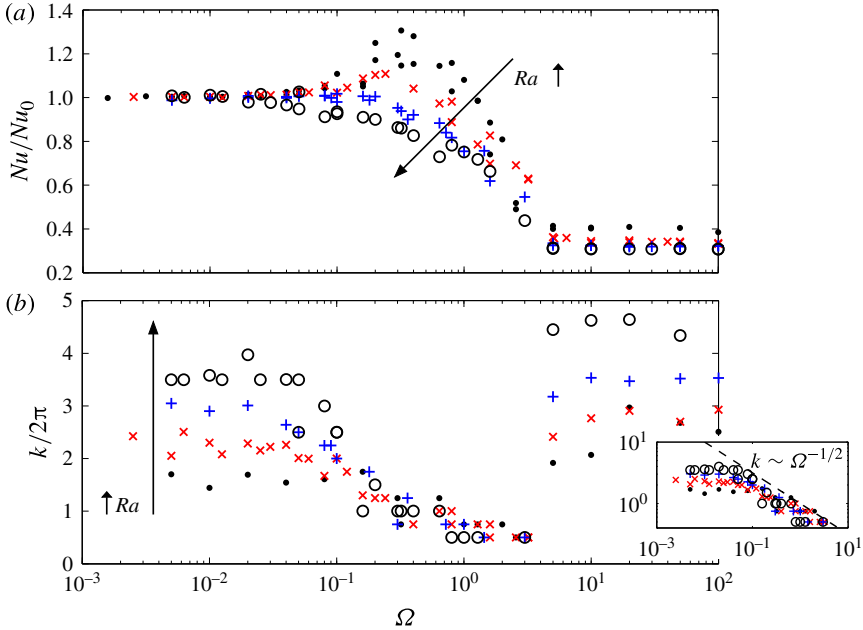
FIGURE 10. (Colour online) Data from reduced simulations for $Ra = 2500$ (dots), $Ra = 5000$ (crosses), $Ra = 10^4$ (pluses) and $Ra = 2 \times 10^4$ (circles). (*a*) The Nusselt number $Nu(\Omega)$, scaled by the Nusselt number Nu_0 for homogeneous convection (from the results of Hewitt *et al.* 2012). (*b*) The time-averaged modal wavenumber k scaled by 2π, as measured from a Fourier transform of the temperature field at $z = 0.5$ for $\Omega < 5$ (the advection regime) and at $z = 0.75$ for $\Omega > 5$ (the diffusion regime). The inset shows the data for $\Omega < 5$ on a log–log scale, together with the scaling $k \sim \Omega^{-1/2}$ (see §4.1 for a theoretical prediction of this scaling). Note that the simulations at $Ra = 2 \times 10^4$ have aspect ratio $L = 2$, rather than $L = 4$.

domain, and the thin downwelling plumes in the lower half of the domain lie below the broad downwelling regions in the upper half of the domain.

3.5. *Dependence on Ra*

We have, thus far, focused on the flow at a fixed value of $Ra = 5000$. Figure 10(*a*) shows calculations of $Nu(\Omega)$ for different values of Ra in the range $2500 \leqslant Ra \leqslant 2 \times 10^4$, scaled by the Nusselt number $Nu_0(Ra)$ for homogeneous Rayleigh–Darcy convection. There are two particularly interesting features of this plot. First, the initial trend in $Nu(\Omega)$ as Ω is increased changes with the value of Ra: for $Ra = 2500$, Nu increases by over 30 % before then decreasing, while for $Ra = 2 \times 10^4$, Nu decreases monotonically. Second, Nu is approximately independent of Ω for $\Omega \gtrsim 5$. This observation can be explained by the fact that the flux across the low-permeability layer is diffusive in this regime, and so is independent of Π. The transition to the diffusion regime appears to occur at a value of Ω that is roughly independent of Ra, which is perhaps surprising given that the Rayleigh number can be interpreted as a measure of the relative strength of advection and diffusion.

Calculation of the time-averaged modal horizontal wavenumber $k(\Omega)$ at $z = 0.5$ (figure 10*b*) gives somewhat noisy data, which reflects the degree of hysteresis that
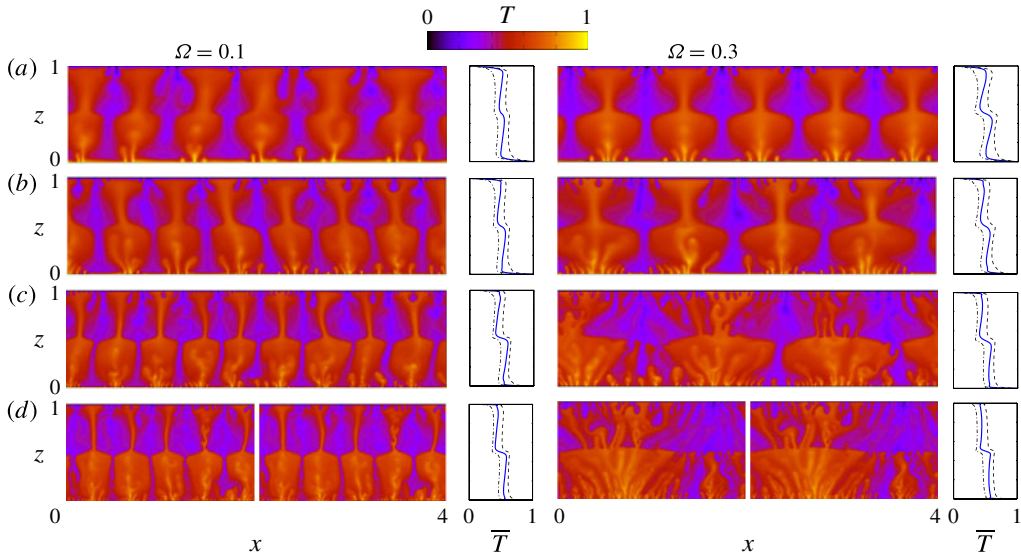
FIGURE 11. (Colour online) Snapshots of the temperature field from reduced simulations for $\Omega = 0.1$ (left) and $\Omega = 0.3$ (right), together with profiles of $\overline{T}(z)$ (solid lines) and the average temperature of fluid with $w > 0$ (dashed lines) and of fluid with $w < 0$ (dot-dashed lines). (*a*) $Ra = 2500$, (*b*) $Ra = 5000$, (*c*) $Ra = 10^4$, and (*d*) $Ra = 2 \times 10^4$. In (*d*), the simulations have an aspect ratio $L = 2$; the snapshot is shown twice for comparison with the other simulations which have $L = 4$.

can affect the flow. For small Ω, the wavenumber tends to the value for homogeneous convection (which is approximately fitted by $k = 0.48Ra^{0.4}$; see figure 4 of Hewitt *et al.* 2012). The wavenumber decreases for $\Omega \gtrsim 0.1$, which roughly coincides with the value of Ω at which Nu/Nu_0 begins to differ appreciably from 1. The subsequent decrease in k can be approximately fitted by a scaling of $k \sim \Omega^{-1/2}$ (figure 10*b* inset).

For $\Omega \gtrsim 5$ in the diffusion regime, the temperature is roughly uniform at $z = 0.5$; in this range we instead measure the average wavenumber k at $z = 0.75$, in the middle of the upper layer. The wavenumber is slightly larger than the wavenumber for homogeneous convection, as can be understood by a simple rescaling of the height and length scales. The flow in each half of the domain resembles homogeneous Rayleigh–Darcy convection in a layer with half the height and half the temperature difference, which gives an effective Rayleigh number four times smaller than Ra and an effective wavenumber that is half the measured value. This rescaling, together with the relationship $k \sim Ra^{0.4}$, suggests that the measured wavenumber should be roughly a factor of $2/4^{0.4} \approx 1.15$ larger than the homogeneous value, and this prediction is consistent with the data shown in figure 10(*b*).

Figure 11 shows a comparison of snapshots of the flow for different values of Ra. For $\Omega = 0.1$, the flow has an ordered cellular structure at each value of Ra, although the dominant horizontal length scale of the flow decreases as Ra is increased, and the asymmetry in the widths of upwelling and downwelling plumes is clearer at larger Ra. For $\Omega = 0.3$, however, the qualitative structure of the flow varies with Ra. In particular, the flow for larger Ra (figure 11*c,d*) is affected by the formation of protoplumes near the interior boundary, and, as a result, the flow appears more disordered than the cellular flow at smaller values of Ra (figure 11*a,b*).

It is interesting to note (with reference to figure 10*a*), that *Nu* increases between $\Omega = 0.1$ and $\Omega = 0.3$ for the lower values of *Ra* (figure 11*a*,*b*), but decreases over this range for the higher values (figure 11*c*,*d*). Based on the observations above, the increase in *Nu* with increasing Ω at moderate *Ra* appears to coincide with an increasingly ordered cellular flow structure. Conversely, the absence of such an increase at higher *Ra* coincides with the growth of protoplume instabilities near the low-permeability layer, which break down the cellular structure and lead to a more disordered flow.

3.6. *Summary of main observations*

We have shown that the dynamics of the statistically steady flow depend only on the ratio $\Omega = h/\Pi$ for h, $\Pi \ll 1$ and for a given value of *Ra*. The horizontal length scale of the flow increases as Ω is increased. For small values of Ω, the structure of the flow resembles homogeneous columnar flow. For larger values of Ω, the flow adopts an ordered cellular structure which, for sufficiently large Ω, is unstable to the formation of protoplumes near the interior boundary. For even larger values of Ω, there is a distinct transition when the advective flux across the inner boundary becomes weaker than the diffusive flux.

For $Ra = 5000$, we found that the Nusselt number initially increases with Ω, to a maximum at $\Omega \approx 0.25$. For larger values of Ω, *Nu* then decreases. Beyond the transition to the diffusion regime at $\Omega \approx 5$, *Nu* is independent of Ω in the reduced model. In full simulations with a finite thickness h of the low-permeability layer, *Nu* continues to decrease in the diffusion regime as h is increased (figure 5).

There are two main differences in this behaviour at different values of *Ra*. First, the initial increase in *Nu* with Ω weakens at larger values of *Ra*, and at $Ra = 2 \times 10^4$ $Nu(\Omega)$ decreases monotonically. Second, as *Ra* is increased, the formation of protoplumes near the inner boundary appears to occur at a lower value of Ω. The decrease in the horizontal wavenumber k over the range of Ω for which *Nu* decreases is roughly fitted by $k \sim \Omega^{-1/2}$ (figure 10*b*). The value of $\Omega \approx 5$ at which there is a transition in the flow to the diffusion regime appears to be roughly independent of *Ra*.

4. Simple theoretical models

In order to develop some understanding of the observed behaviour of $Nu(\Omega)$, in this section we describe simple one-dimensional models of the statistically steady convective system. These models provide a tentative basis for interpretation of the dynamical behaviour that we have observed, but further refinement will be required for a fuller understanding (see § 4.3). We describe two simple models, one for each of the regimes identified in § 3: first, in § 4.1, for the advection regime ($\Omega \lesssim 5$); and second, in § 4.2, for the diffusion regime ($\Omega \gtrsim 5$).

For simplicity, we make the assumption in both models that the horizontally averaged temperature $\overline{T}$ is approximately uniform in each of the upper and lower layers of the domain, except in thin boundary regions near $z = 0$, $z = 0.5$ and $z = 1$. (This approximation neglects any background stratification.) Recalling the symmetry of the system about $z = 0.5$, we therefore set

$$\overline{T} = \Theta(\Omega) \quad \text{in } z > 0.5, \quad \text{and} \quad \overline{T} = 1 - \Theta(\Omega) \quad \text{in } z < 0.5. \qquad (4.1a,b)$$
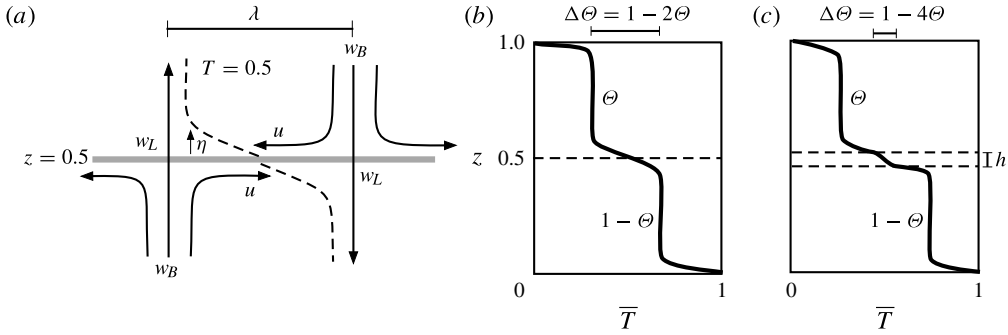
FIGURE 12. Schematic diagrams of the model system. (*a*) A sketch of the flow (solid curves) through and near the low-permeability layer in the advection regime (see §4.1), and the isotherm along which $T = 0.5$ (dashed curve). (*b*) A profile of the horizontally averaged temperature $\overline{T}$ for the advection regime. (*c*) A profile of $\overline{T}$ for the diffusion regime.

Hewitt *et al.* (2013) found that, in a homogeneous layer of unit depth with average interior temperature $\overline{T} = 0.5$, the convective heat flux Nu is well described for $Ra \gtrsim 1300$ by the empirical parameterization $Nu = \alpha Ra + \beta$, where $\alpha = 6.9 \times 10^{-3}$ and $\beta = 2.75$. A simple rescaling of the depth and temperature scales in the definitions of Nu and Ra allows the heat flux through a layer of depth $\widehat{H}$ with average interior temperature Θ to be described by

$$Nu = 4\alpha\Theta^2 Ra + 2\beta\frac{\Theta}{\widehat{H}}, \tag{4.2}$$

where α and β are given above. We use (4.2) to parameterize the convective flux through the upper and lower layers in the models outlined below.

4.1. *Advective transport across the low-permeability layer*

Figure 12(*a*) shows a schematic diagram of the flow in the advection regime. In the upper and lower layers, we model the flow as a series of circulating cells of depth $1/2$ and width λ. Broad downwelling (upwelling) flow in the upper (lower) layer with typical vertical velocity w_B impinges on the low-permeability layer, and either 'leaks' through the layer with typical velocity w_L or spreads laterally with typical velocity u (figure 12*a*).

The leakage velocity w_L is driven by the vertical pressure difference $[p]$ across the low-permeability layer, which, owing to the symmetry of the system, is also the horizontal pressure difference over the distance λ between neighbouring plumes. From the vertical component of Darcy's law inside the layer and the horizontal component outside the layer, we therefore have

$$[p] \sim \Omega w_L \sim u\lambda \tag{4.3}$$

(cf. (3.3)). Calculated values of w_L, u and λ from simulations give good agreement with (4.3).

The pressure difference $[p]$ must also be related to the density contrasts between the upper and lower layers. Just above the low-permeability layer, relatively hot

fluid of temperature $\sim 1 - \Theta$ that has leaked from below spreads laterally beneath relatively cold fluid of temperature $\sim \Theta$. We model this lateral flow as a thin buoyant boundary layer of hot fluid which is driven by a hydrostatic pressure difference

$$[p] \sim \Delta \Theta \eta, \tag{4.4}$$

where η is the depth of the boundary layer (figure 12a) and $\Delta \Theta = 1 - 2\Theta$ is the density difference between the hot and cold fluid (figure 12b). Under the assumption that advection dominates the flow near to the low-permeability layer, so that diffusion can be neglected, we deduce that η is an isotherm (figure 12a) with a slope $\sim \eta / \lambda$ set by the relative strength of vertical and horizontal flow. Hence

$$\frac{\eta}{\lambda} \sim \frac{w_L}{u}. \tag{4.5}$$

The velocities w_L and u are also related to the typical vertical velocity w_B of the broad downwelling or upwelling regions by conservation of volume flux, which gives

$$u \sim (w_B - w_L) \lambda. \tag{4.6}$$

Equations (4.3)–(4.6) provide five scaling relationships which describe the unknown variables u, w_L, $[p]$, λ and η in terms of $\Delta \Theta$, Ω, and w_B. The equations combine to give $w_B - w_L \sim \Delta \Theta / \Omega$ and a simple scaling of

$$w_L \sim \Theta - \nu \frac{\Delta \Theta}{\Omega}, \tag{4.7}$$

for the leakage velocity w_L, where ν is an undetermined constant of proportionality and $w_B \sim \Theta$ by Darcy's law.

We close the system by balancing the leakage heat flux $\sim Ra\, w_L \Delta \Theta$ through the low-permeability layer with the convective heat flux in the upper and lower layer given by (4.2). Such a balance gives a quadratic equation for Θ of the form

$$4\alpha \Theta^2 + \frac{2\beta \Theta}{Ra} = \gamma (1 - 2\Theta) \left[\Theta - \nu \frac{(1 - 2\Theta)}{\Omega} \right], \tag{4.8}$$

where γ is another constant of proportionality. (Note that we have set the depth scale $\widehat{H}$ in (4.2) to unity in order that Nu reduces to the homogeneous value for small Ω.)

Equation (4.8) can be readily solved for Θ (the resultant expression is convoluted and not given here) and has one real root in the range $0 \leqslant \Theta \leqslant 1/2$ if $\Omega > O(\nu \alpha / \gamma)$. In fact, since $\alpha = O(10^{-3})$ and $Ra \geqslant O(10^3)$, (4.8) can be well approximated by setting the left-hand side equal to zero, provided that $\gamma = O(1)$ or larger. The simple solution of the resultant equation is given by

$$\Theta = (2 + \Omega / \nu)^{-1}, \tag{4.9}$$

which can be combined with (4.2) to give an expression for the flux of the form

$$Nu = \frac{\alpha Ra}{(1 + \Omega / 2\nu)^2} + \frac{\beta}{(1 + \Omega / 2\nu)}. \tag{4.10}$$

The predictions of $Nu(\Omega)$ from (4.10) for $\nu = 3$ are shown in figure 13, and give a reasonably good qualitative fit with the data. The parameter ν was chosen to give
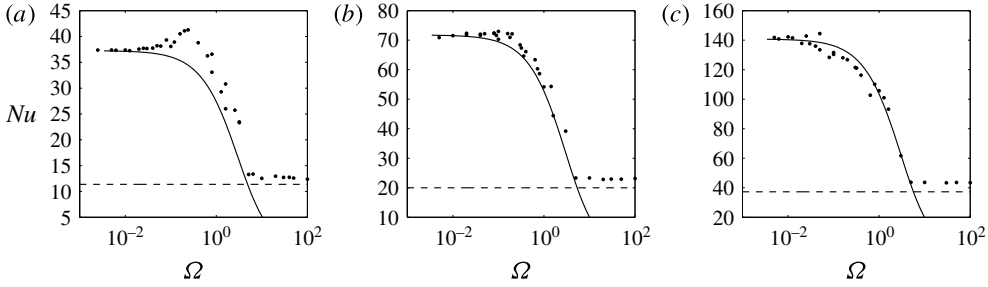
FIGURE 13. A comparison of calculations of $Nu(\Omega)$ from reduced simulations (dots) and the predictions of the model for the advection regime with $\nu = 3$ (solid lines, from (4.10)) and for the diffusion regime (dashed lines, from (4.14b)). (a) $Ra = 5000$, (b) $Ra = 10^4$, and (c) $Ra = 2 \times 10^4$.

a rough fit across the range of Ra. The model does not describe the initial increase in Nu with Ω at moderate values of Ra (e.g. in figure 13a).

The model also gives a prediction for the scaling of the width λ of the cells. Equations (4.3)–(4.5) combine to give $w_L \sim \Delta\Theta\lambda^2/\Omega^2$, which can then be combined with (4.7) to give

$$\lambda \sim \left(\Omega^2 \frac{\Theta}{\Delta\Theta} - \nu\Omega \right)^{1/2} \sim \Omega^{1/2}, \tag{4.11}$$

using (4.9). The model therefore predicts that the length scale between plumes increases like $\Omega^{1/2}$, or, equivalently, the horizontal wavenumber decreases like $\Omega^{-1/2}$, in agreement with the calculations of the wavenumber k from the numerical data, shown in figure 10(b).

4.2. *Diffusive transport across the low-permeability layer*

For sufficiently large values of Ω, the flux through the low-permeability layer is primarily diffusive. In the diffusion regime, the system resembles two layers of homogeneous columnar convection placed one on top of the other, with boundary-layer regions above and below the low-permeability layer as well as near the upper and lower boundaries of the domain (figure 12c).

The diffusive flux across the low-permeability layer of thickness h is given by

$$Nu \approx \frac{\Delta\Theta}{h} = \frac{1 - 4\Theta}{h} \tag{4.12}$$

(figure 12c). We eliminate Θ by equating (4.12) with the convective flux through the upper and lower layers, which is given by (4.2) with $\widehat{H} = 1/2$. The resultant quadratic equation for $\Theta(h)$ has one real root in the range $0 \leqslant \Theta \leqslant 1/2$, which can be back-substituted into (4.12) to give

$$Nu = \frac{1}{\alpha Ra \, h^2} \left[(\alpha Ra + 2\beta) \, h + 2 - 2\sqrt{\alpha \, Ra \, h + (1 + \beta h)^2} \right]. \tag{4.13}$$

The prediction of $Nu(h)$ from (4.13) was shown by the solid line in figure 4(a); it shows that Nu decreases as h is increased, and gives very good agreement with numerical results for $\Pi = 0$.

For $h, \Pi \ll 1$, the interior temperature and Nusselt number from (4.13) reduce to

$$\Theta = \tfrac{1}{4} - O(h) \quad \text{and} \quad Nu = \tfrac{1}{4}\alpha\, Ra + \beta - O(h). \qquad (4.14a,b)$$

Thus, in the limit $h, \Pi \to 0$, Nu is a constant. Predictions of (4.14b) give fairly good agreement with data from reduced simulations at large Ω (figure 13, dashed lines), although they appear to slightly underestimate the data. It is likely that this underestimate is related to the implicit assumption in the model that the temperature at the edge of the low-permeability layer is uniform. In the reduced simulations, we observed non-zero horizontal fluctuations in T at $z = 0.5$ (figure 7d), which will induce flow, potentially leading to thinner diffusive boundary layers above and below the low-permeability layer and a slightly larger flux than the model predicts.

4.3. *Discussion*

The results of figure 13 demonstrate that simple one-dimensional models can give a reasonable qualitative description of the relationship $Nu(\Omega)$. The model for the advection regime also predicts that the dominant horizontal wavenumber decreases like $\Omega^{-1/2}$, in agreement with the numerical data shown in figure 10(b). The model is based on a number of assumptions, and some of these are briefly discussed here.

The model takes the form of a balance between the heat flux through the upper and lower layers and the heat flux through the low-permeability layer, each of which is parameterized in terms of the average temperature in each half of the domain. The heat flux through the upper and lower layers is related to the convective flux for homogeneous Rayleigh–Darcy convection by a rescaling of temperatures and lengths. The model for the heat flux through the low-permeability layer has three key components: a relationship between the pressure-driven vertical flow across the layer and horizontal flow above and below the layer (4.3); a relationship between the pressure and the temperature difference across the layer (4.4), which incorporates an expression for the boundary-layer depth near to the layer (4.5); and conservation of volume flux (4.6).

The second relationship is the least straightforward to model. In order to generate a simple closed model, we assumed that heat is advected without diffusing near to the low-permeability layer, which gives rise to the scaling in (4.5). Inspection of isotherms and streamlines from the numerical simulations suggests that vertical diffusion may not be completely negligible in these regions; however, it is not clear how to incorporate a balance between diffusion and both horizontal and vertical advection into the simple model.

The boundary-layer scaling in (4.4) relies on the assumption that the lateral flow on either side of the layer is not weak relative to the vertical flow across the layer. This assumption breaks down in the limit $\Omega \to 0$, as the homogeneous flow is predominantly vertical throughout the interior of the domain. In fact, we find that there are no real solutions to (4.8) if Ω is sufficiently small $(\Omega < O(\nu\alpha/\gamma))$, which probably reflects the breakdown of this assumption.

The observed increase in Nu with Ω for small Ω is not captured by the simple model in the advection regime. Our numerical results suggest that the increase in Nu is related to the flow becoming more 'ordered' (see e.g. figure 6), although this is a qualitative observation and it is not clear how an increased 'order' leads to an increased flux. An additional interesting feature of the increase in Nu is that the effect is smaller at larger values of Ra, and so, by implication, it is not associated with asymptotically large values of Ra. We have been unable to find a simple physical model for the increase in Nu with Ω, and the effect remains puzzling.

5. Conclusions

We have undertaken a detailed numerical investigation of statistically steady convection at high Ra in a domain containing an interior low-permeability layer of height h and relative permeability $\Pi < 1$. In the limit $h, \Pi \ll 1$, the flow depends only on the parameter $\Omega = h/\Pi$, and the low-permeability layer can be parameterized by a jump condition for the horizontal velocity at $z = 0.5$. Reduced numerical simulations which solve the jump condition give good agreement with fully resolved numerical simulations for a range of values of h and Π.

In §3.4, we examined the structure of the flow for $Ra = 5000$, in the reduced framework $h, \Pi \ll 1$. For $\Omega \gtrsim 0.05$, the flow develops an ordered cellular structure with a horizontal length scale that increases with Ω. Each cell is roughly half the height of the domain, and comprises a thin vertical plume carrying fluid in one direction and a much wider plume carrying the return flow, together with some 'leakage' of buoyancy across the low-permeability layer. Remarkably, Nu increases as Ω is increased (i.e. as the permeability of the interior layer is decreased) in this dynamical regime. For $0.3 \lesssim \Omega \lesssim 5$, the horizontal length scale of the flow continues to increase but Nu decreases. The flow can be unstable to the formation of protoplumes near the low-permeability layer in this range of Ω. For $\Omega \gtrsim 5$, advection through the low-permeability layer is weaker than diffusion, and the flow structure changes completely to resemble two layers of homogeneous columnar convection placed one on top of the other. The statistically steady flow structure and the associated flux appear to be sensitively affected by the initial conditions, which is probably due to restriction imposed on the flow by the horizontal periodicity of the domain.

In §3.5, we explored the dependence of this behaviour on Ra. We found that the initial increase in Nu with Ω is more pronounced at smaller Ra and less pronounced at larger Ra. As Ra is increased, the value of Ω above which the flow near the low-permeability layer is unstable to the growth of protoplumes appears to decrease. Calculations from numerical simulations of the dominant horizontal wavenumber k at $z = 0.5$ suggest that the increase in the horizontal length scale with Ω roughly fits a scaling of $k \sim \Omega^{-1/2}$.

In §4, we developed simple one-dimensional models that describe the behaviour of $Nu(\Omega)$, for both the advection and the diffusion regime. The model for the advection regime also predicts that the dominant horizontal wavenumber scales with $\Omega^{-1/2}$, in agreement with the numerical data. This model was discussed in §4.3. The model for the diffusion regime has no free parameters and gives fairly good agreement with both full and reduced numerical results.

Throughout this paper, we have considered a low-permeability layer located at the centre of the cell, with upper and lower layers of equal depth. An interesting extension to this work would be to examine the effect of a low-permeability layer located at different depths in the cell, which would break the reflectional symmetry of the system about $z = 0.5$. A simple balance between the effective Rayleigh numbers of the upper and lower layers, each of which should scale with the height and temperature difference across the layer, suggests that the heat flux should decrease if the low-permeability layer is moved off centre. The dominant horizontal length scale of the flow is also likely to vary as the location of the low-permeability layer is changed, although whether the length scale increases or decreases may depend on whether the deeper or the shallower layer dominates the dynamics of the flow. A detailed examination of the effects of the location of the low-permeability layer lies beyond the scope of this paper and is left for future work.

Two observations from this work are particularly striking: the dramatic increase in the horizontal length scale of the flow with Ω, and the unexpected increase in Nu with Ω for moderate values of Ra. These observations could have interesting consequences in geophysical and industrial settings.

Appendix A. Discussion of the assumptions of uniform porosity and thermal diffusivity

For simplicity, in the main body of this paper we made the assumption that the porosity ϕ is uniform throughout the domain, and is, by implication, independent of the permeability K. In a physical system, it is likely that ϕ would vary with K. However, typical models of the relationship $K(\phi)$ (such as the Kozeny–Carman model) suggest that the porosity scales with roughly the cube root of the permeability (Bear 1988), and so changes in the porosity are likely to be much weaker than changes in the permeability. The average thermal diffusivity κ, which we assumed to be constant, is in general a weighted average of the thermal conductivities k_s and k_l in the solid and liquid phases, scaled by $\rho_l c_l$, and so will also vary with the porosity if $k_s \neq k_l$.

Here we briefly consider the qualitative effect of a lower porosity in the low-permeability layer. Suppose that the porosity and thermal diffusivity of the upper and lower layers are ϕ_1 and κ_1, respectively, while those of the low-permeability layer are $\phi_2 < \phi_1$ and κ_2, respectively. The flow $\boldsymbol{u}$ is determined by the solution of the Poisson equation (2.3b), and is thus not directly dependent on the porosity or diffusivity. Under the assumption that the flow through the low-permeability layer is not dominated by time-dependent dynamics, the advective flux through the layer, which scales with wT, is also not significantly affected by a decrease in the porosity. The diffusive flux, however, is scaled by a factor of κ_2/κ_1 (see (2.1d)). The relative size of κ_1 and κ_2 depends on the conductivities k_s and k_l as well as on the porosity: a decrease in porosity will lead to an increase in the proportion of the heat flux that diffuses through the solid phase of the medium.

Thus, we anticipate that a lower porosity in the low-permeability layer would not have an appreciable effect on the flux in the advection regime, but could lead to either a larger or a smaller flux in the diffusion regime, depending on the relative sizes of k_s and k_l. As a result, the transition between advection and diffusion regimes may occur at a different value of Ω. A simple parameterization of the effect of a lower porosity in the low-permeability layer could be incorporated into our model of the flux in the diffusion regime (§ 4.2) by including a factor of κ_2/κ_1 in (4.12); this parameterization is equivalent to the rescaling $h \rightarrow (\kappa_1/\kappa_2)\, h$.

Appendix B. Numerical scheme

In this appendix, we outline the numerical scheme that we used for both 'full' and 'reduced' simulations. The numerical scheme is similar to that used by Hewitt *et al.* (2012, 2013).

In order to resolve the dynamics in the thin boundary layers near to the upper and lower boundaries of the domain and near to the low-permeability layer, we used a vertical coordinate transformation $\zeta(z)$. For the full simulations, we used a coordinate transformation of the form

$$z(\zeta) = \frac{\mathscr{T}(\zeta, 0.25+\nu, \eta_1) + \mathscr{T}(\zeta, 0.75-\nu, \eta_1) + \varepsilon\mathscr{T}(\zeta, 0.5, \eta_2)}{\mathscr{T}(1, 0.25+\nu, \eta_1) + \mathscr{T}(1, 0.75-\nu, \eta_1) + \varepsilon\mathscr{T}(1, 0.5, \eta_2)}, \qquad \text{(B 1)}$$

where

$$\mathcal{T}(x, y, \eta) = \tanh\left[\eta\,(x-y)\right] + \tanh\,(\eta y), \tag{B 2}$$

and η_1, η_2, ν and ε are specified parameters that depend on the thickness h and on Ra. These parameters were chosen to ensure that sufficient grid points lay in the regions near $z = z_1$ and $z = z_2$, as well as in the boundary layers near $z = 0$ and $z = 1$.

For the reduced simulations, we used a simpler transformation of the form

$$z(\zeta) = \frac{\mathcal{T}\,(\zeta, 0.25 + \nu, \eta) + \mathcal{T}\,(\zeta, 0.75 - \nu, \eta)}{\mathcal{T}\,(1, 0.25 + \nu, \eta) + \mathcal{T}\,(1, 0.75 - \nu, \eta)}, \tag{B 3}$$

where $\mathcal{T}$ is defined in (B 2), and $\eta(\Omega, Ra)$ and $\nu(\Omega, Ra)$ are again parameters that control the stretching, chosen to ensure the dynamics near $z = 0$, $z = 0.5$, and $z = 1$ were fully resolved.

After an analytic transformation to (x, ζ) coordinates, the governing equations (2.3c) and (2.7) for both full and reduced simulations were solved on a uniform rectangular grid. The transport equation (2.3c) was discretized in time with a second-order alternating-direction implicit (ADI) method (Press *et al.* 1989). The diffusion and advection operators were spatially discretized with standard second-order finite differences and a second-order flux-conservative representation, respectively. The Poisson equation (2.7) was solved for the streamfunction ψ, and thus the velocity $\boldsymbol{u}$, using a fast Fourier transform for the x derivatives and a standard second-order finite-difference operator for the ζ derivative. The ADI method requires the values of the velocity at the half time step, which were calculated using a second-order midpoint method.

In the full simulations, both the transport equation and the Poisson equation were solved across the whole domain. In the reduced simulations, the velocity at $z = 0.5$ was given by the jump condition (3.3), which was incorporated into the numerical scheme by replacing the expression for the streamfunction at $z = 0.5$ from the Poisson equation with an expression derived from (3.3). Since the temperature is continuous at $z = 0.5$, the transport equation was again solved across the whole domain.

For the full simulations at $Ra = 5000$, we used a typical spatial resolution of $\Delta x = (512)^{-1}$ and $\Delta \zeta = (350)^{-1}$ for the horizontal and vertical directions, respectively. For the reduced simulations, we used a smaller vertical resolution of $\Delta \zeta = (220)^{-1}$. The time step was chosen to be smaller than the Courant time scale. We confirmed that the calculations were well resolved by doubling both the spatial and temporal resolutions and recovering statistically identical results. Based on previous calculations of the homogeneous layer (Hewitt *et al.* 2012), we expected that the smallest horizontal scales decreased like Ra^{-1}, and so a scaling of $\Delta x \sim Ra^{-1}$ was used for simulations at other values of Ra.

REFERENCES

BACHU, S. 2008 CO_2 storage in geological media: role, means, status and barriers to deployment. *Prog. Energy Combust. Sci.* **34**, 254–273.

BACKHAUS, S., TURITSYN, K. & ECKE, R. E. 2011 Convective instability and mass transport of diffusion layers in a Hele-Shaw geometry. *Phys. Rev. Lett.* **106**, 104501.

BEAR, J. 1988 *Dynamics of Fluids in Porous Media*. Dover.

BICKLE, M., CHADWICK, A., HUPPERT, H. E., HALLWORTH, M. A. & LYLE, S. 2007 Modelling carbon dioxide accumulation at Sleipner: implications for underground carbon storage. *Earth Planet. Sci. Lett.* **255**, 164–176.

DANIEL, D., TILTON, N. & RIAZ, A. 2013 Optimal perturbations of gravitationally unstable, transient boundary layers in porous media. *J. Fluid Mech.* **727**, 456–487.

ENNIS-KING, J. P., PRESTON, I. & PATERSON, L. 2005 Onset of convection in anisotropic porous media subject to a rapid change in boundary conditions. *Phys. Fluids* **17**, 84107–84115.

FRIEDLINGSTEIN, P., HOUGHTON, R. A., MARLAND, G., HACKLER, J., BODEN, T. A., CONWAY, T. J., CANADELL, J. G., RAUPACH, M. R., CIAIS, P. & LE QUERE, C. 2010 Update on CO_2 emission. *Nat. Geosci.* **3**, 811–812.

GENÇ, G. & REES, D. A. S. 2011 The onset of convection in horizontally partitioned porous layers. *Phys. Fluids* **23**, 064107.

GILFILLAN, S. M. V., SHERWOOD LOLLAR, B., HOLLAND, G., BLAGBURN, D., STEVENS, S., SCHOELL, M., CASSIDY, M., DING, Z., ZHOU, Z., LACRAMPE-COULOUME, G. & BALLENTINE, C. J. 2009 Solubility trapping in formation water as dominant CO_2 sinks in natural gas fields. *Nature* **458**, 614–618.

GRAHAM, M. D. & STEEN, P. H. 1994 Plume formation and resonant bifurcations in porous-media convection. *J. Fluid Mech.* **272**, 67–89.

HEWITT, D. R., NEUFELD, J. A. & LISTER, J. R. 2012 Ultimate regime of high Rayleigh number convection in a porous medium. *Phys. Rev. Lett.* **108**, 224503.

HEWITT, D. R., NEUFELD, J. A. & LISTER, J. R. 2013 Convective shutdown in a porous medium at high Rayleigh number. *J. Fluid Mech.* **719**, 551–586.

HEWITT, D. R., NEUFELD, J. A. & LISTER, J. R. 2014 High Rayleigh number convection in a three-dimensional porous medium. *J. Fluid Mech.* **748**, 879–895.

HUPPERT, H. E. & NEUFELD, J. A. 2014 The fluid mechanics of carbon dioxide sequestration. *Annu. Rev. Fluid Mech.* **46**, 255–272.

KNEAFSEY, T. J. & PRUESS, K. 2010 Laboratory flow experiments for visualizing carbon dioxide-induced, density-driven brine convection. *Transp. Porous. Med.* **82**, 123–139.

LAPWOOD, E. R. 1948 Convection of a fluid in a porous medium. *Math. Proc. Camb. Phil. Soc.* **44**, 508–521.

MCKIBBIN, R. & O'SULLIVAN, M. J. 1980 Onset of convection in a layered porous medium heated from below. *J. Fluid Mech.* **96**, 375–393.

MCKIBBIN, R. & O'SULLIVAN, M. J. 1981 Heat transfer in a layered porous medium heated from above. *J. Fluid Mech.* **111**, 141–173.

MCKIBBIN, R. & TYVAND, P. A. 1983 Thermal convection in a porous medium composed of alternating thick and thin layers. *Intl J. Heat Mass Transfer* **26**, 761–780.

MONKHOUSE, F. J. 1970 *Principles of Physical Geography*. University of London Press.

MORRIS, K. A. & SHEPPERD, C. M. 1982 The role of clay minerals in influencing porosity and permeability characteristics in the Bridport sands of Wytch Farm, Dorset. *Clay Miner.* **17**, 41–54.

NEUFELD, J. A., HESSE, M. A., RIAZ, A., HALLWORTH, M. A., TCHELEPI, H. A. & HUPPERT, H. E. 2010 Convective dissolution of carbon dioxide in saline aquifers. *Geophys. Res. Lett.* **37**, L22404.

NEUFELD, J. A., VELLA, D., HUPPERT, H. E. & LISTER, J. R. 2011 Leakage from gravity currents in a porous medium. Part 1. A localized sink. *J. Fluid Mech.* **666**, 391–413.

NIELD, D. A. & BEJAN, A. 2013 *Convection in Porous Media*, 4th edn. Springer.

OTERO, J., DONTCHEVA, L. A., JOHNSTON, H., WORTHING, R. A., KURGANOV, A., PETROVA, G. & DOERING, C. R. 2004 High-Rayleigh-number convection in a fluid-saturated porous layer. *J. Fluid Mech.* **500**, 263–281.

PAU, G. S. H., BELL, J. B., PRUESS, K., ALMGREN, A. S., LIJEWSKI, M. J. & ZHANG, K. 2010 High-resolution simulation and characterization of density-driven flow in CO_2 storage in saline aquifers. *Adv. Water Resour.* **33**, 443–455.

PHILLIPS, O. M. 2009 *Geological Fluids Dynamics*. Cambridge University Press.

PRESS, W. H., FLANNERY, B. P., TEUKOLSKY, S. A. & VETTERLING, W. T. 1989 *Numerical Recipes (Fortran)*, 1st edn. Cambridge University Press.

PRITCHARD, D. 2007 Gravity currents over fractured substrates in a porous medium. *J. Fluid Mech.* **584**, 415–431.

RAPAKA, S., PAWAR, R. J., STAUFFER, P. H., ZHANG, D. & CHEN, S. 2009 Onset of convection over a transient base-state in anisotropic and layer porous media. *J. Fluid Mech.* **641**, 227–244.

REES, D. A. S. & RILEY, D. S. 1990 The three-dimensional stability of finite-amplitude convection in a layered porous medium heated from below. *J. Fluid Mech.* **211**, 437–461.

RIAZ, A., HESSE, M. A., TCHELEPI, H. A. & ORR, F. M. JR 2006 Onset of convection in a gravitationally unstable diffusive layer in porous media. *J. Fluid Mech.* **548**, 87–111.

SIMMONS, C. T., FENSTEMAKER, T. R. & SHARP, J. M. 2001 Variable-density groundwater flow and solute transport in heterogeneous porous media: approaches, resolutions and future challenges. *J. Contam. Hydrol.* **52**, 245–275.

SLIM, A. C. 2014 Solutal convection regimes in a two-dimensional porous medium. *J. Fluid Mech.* **741**, 461–491.

SLIM, A. C., BANDI, M. M., MILLER, J. C. & MAHADEVAN, L. 2013 Dissolution-driven convection in a Hele-Shaw cell. *Phys. Fluids* **25**, 024101.

STERNLOF, K. R., KARIMI-FARD, M., POLLARD, D. D. & DURLOFSKY, L. J. 2006 Flow and transport effects of compaction bands in sandstones at scales relevant to aquifer and reservoir management. *Water Resour. Res.* **42**, W07425.

SZULCZEWSKI, M. L., HESSE, M. A. & JUANES, R. 2013 Carbon dioxide dissolution in structural and stratigraphic traps. *J. Fluid Mech.* **736**, 287–315.

TILTON, N. & RIAZ, A. 2014 Nonlinear stability of gravitationally unstable, transient, diffusive boundary layers in porous meda. *J. Fluid Mech.* **745**, 251–278.

VELLA, D., NEUFELD, J. A., HUPPERT, H. E. & LISTER, J. R. 2011 Leakage from gravity currents in a porous medium. Part 2. A line sink. *J. Fluid Mech.* **666**, 414–427.

ZHANG, W. 2013 Density-driven enhanced dissolution of injected CO_2 during long-term CO_2 storage. *J. Earth Syst. Sci.* **122**, 1387–1397.